Shang *et al. Respiratory Research* (2025) 26:285
https://doi.org/10.1186/s12931-025-03359-7

Respiratory Research

RESEARCH Open Access

Monocyte-derived macrophages support alveolar regeneration via oncostatin M post-H1N1 infection during the recovery phase

Xiao Shang[1], Ju Jia[2], Jiapei Yu[3,4], Shumei Zou[5], Zeyi Wang[4], Jiuyang Xu[3,4], Hui Li[3,4*] and Bin Cao[1,3,4*]

Abstract

Background Severe influenza virus infection often triggers acute lung injury, and the efficacy of respiratory functional recovery critically depends on timely alveolar regeneration. However, the cellular dynamics and regulatory mechanisms underlying post-infectious alveolar repair remain incompletely understood.

Methods Utilizing *Sftpc-CreER; Rosa26*-mTmG lineage-tracing model, we determine the main stem cell population responsible for alveolar regeneration following influenza-induced injury. Through integrated single-cell RNA sequencing (scRNA-seq), immunofluorescence, and electron microscopy approaches, we mapped cellular transcriptional landscapes and spatial interactions. Key macrophage-epithelial crosstalk was further investigated via in vitro co-culture systems and in vivo conditional depletion models using diphtheria toxin receptor-transgenic mice. Putative regulatory factors were predicted through ligand-receptor interaction analysis and functionally validated in ex vivo organoid models.

Results In this study, we revealed that the severely damaged alveolar barrier after influenza virus infection was rebuilt by the proliferation and differentiation of residual type II alveolar epithelial (AT2) cells in an inflammatory niche. In particular, monocyte-derived macrophage (Mo-Macs) expand, displaying intimate spatial proximity with AT2 cells. In addition, the cellular transcriptional status determined by scRNA-seq revealed that Mo-Macs regulate epithelial cell proliferation. Mo-Macs promoted the formation of AT2 spheres in vitro. Moreover, Mo-Mac depletion resulted in delayed repair of the alveolar epithelial structure in vivo. In addition, the mechanism by which Mo-Macs regulate alveolar epithelial repair involves the secretion of oncostatin M (OSM), which stimulates p-STAT3 activation and promotes AT2 cell proliferation.

Conclusions Our findings revealed that residual AT2 cells act as stem cells in the alveolus and are regulated by Mo-Macs through OSM secretion. These findings increase our understanding of the role of inflammatory signals in regulating tissue repair after severe injury, which may provide a potential avenue for therapeutic intervention in recovered patients.

Keywords Monocyte-derived macrophages, Alveolar regeneration, ScRNA-seq, Oncostatin M

---

*Correspondence:
Hui Li
lihui123000@126.com
Bin Cao
caobin_ben@163.com

Full list of author information is available at the end of the article

Graphical abstract

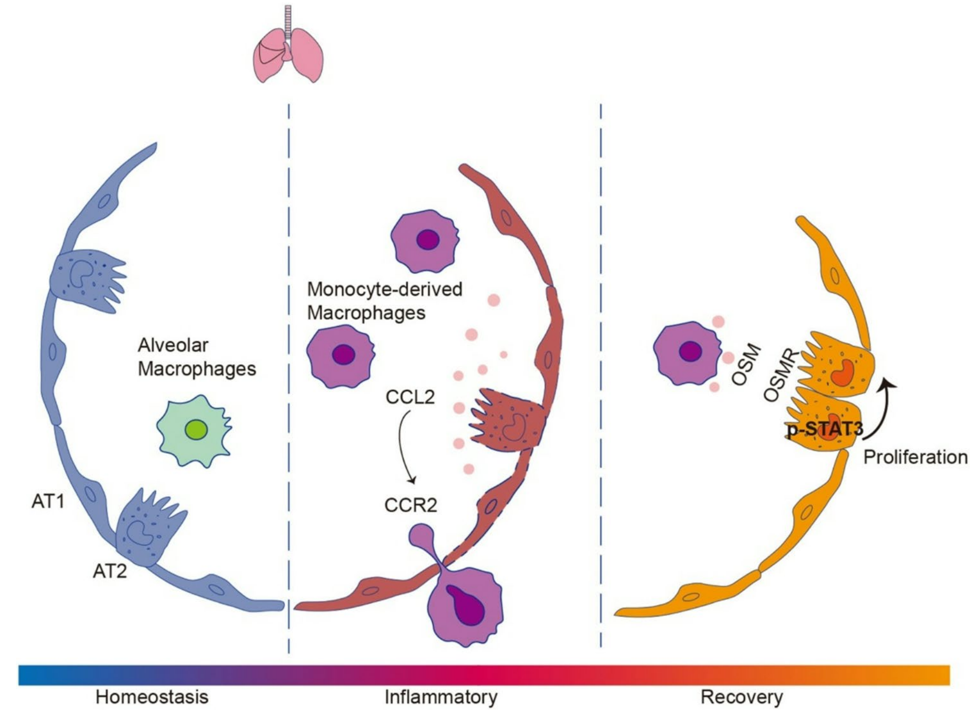

Background

Severe influenza virus infection leads to extensive alveolar epithelial cell death due to both direct viral attack and immune-mediated damage, resulting in gas exchange impairment and disruption of the immune barrier [1–3]. Our preliminary data indicate that alveolar function remains incompletely restored even three months post-discharge following influenza pneumonia [4].

Previous studies have shown that alveolar regeneration following lung injury depends on the rapid proliferation and differentiation of type II alveolar epithelial cells (AT2) [5]. The stem cell function of AT2 cells is regulated by a complex network of signaling pathways, which includes both intrinsic mechanisms and extrinsic factors derived from fibroblasts or immune cells [6]. However, the cellular communication mechanisms driving the regeneration process after severe lung injury remain only partially understood, especially with respect to the role of inflammatory cells in tissue recovery. Immune cells such as group 3 innate lymphoid cells and regulatory T cells have been shown to promote lung repair [7–9]. Inflammatory factors such as IL-1β, TNF-α, and IL-6 are also known to stimulate the proliferation of AT2 cells [10, 11]. On the other hand, antiviral cytokines, including type I interferons (IFN-α and IFN-β) and type III interferons (IFN-λ), disrupt lung epithelial repair [12, 13]. Therefore, a well-regulated inflammatory response is essential not only for defending the host against pathogens but also for facilitating alveolar regeneration.

Macrophages play important roles in maintaining lung homeostasis and regulating tissue repair and fibrosis [14]. Alveolar macrophages (AMs) residing in the alveolar space are derived from the fetal liver and self-renew under healthy conditions. In response to lung injury, monocyte-derived macrophages (Mo-Macs) tend to replace tissue-resident AMs. The infiltration of Mo-Macs is mediated by the CCL2−CCR2 signaling pathway [15] and is associated with severe lung pathology [16]. Recent studies have suggested that Mo-Macs are also involved in regeneration and fibrosis following severe lung injury [17]. Mo-Macs express profibrotic genes [18] and are strongly associated with lung fibrosis in COVID-19 patients [19]. Studies have shown that Mo-Macs can facilitate alveolar regeneration after pneumonectomy and that Ly6G$^+$ monocytes promote alveolar regeneration after acute lung injury [20]. However, the function and underlying mechanism of Mo-Macs in alveolar regeneration post-H1N1 infection remain to be elucidated.

Using single-cell RNA sequencing (scRNA-seq) analysis, mouse genetics, and an alveolar organoid model, this study explored the function and molecular mechanisms of infiltrated immune cells in regulating alveolar repair. These findings demonstrated that Mo-Macs promote alveolar epithelial cell proliferation and tissue recovery. Immunofluorescence staining and transmission electron microscopy revealed that macrophages reside in the alveolar repair region. The in vitro 3D alveolar sphere coculture model confirmed that Mo-Macs can promote AT2 sphere formation. Using CCR2-DTR-GFP mice for DT-mediated cell depletion, the results revealed that Mo-Macs are indispensable for lung recovery. Cell-cell interaction analysis revealed that the Mo-Mac-secreted cytokine oncostatin M (OSM) can bind to its receptor OSMR/IL6st, which is expressed in AT2 cells. The in vitro culture model confirmed that OSM promoted AT2 cell sphere formation via the JAK/STAT3 signaling pathway. Overall, this study provides a comprehensive description of disease progression following severe H1N1 infection and elucidates the function and regulatory mechanisms of Mo-Macs in promoting alveolar regeneration after H1N1 infection.

Methods

Study approvals

The animal experiments were approved by the Key Laboratory for Medical Virology, Chinese Center for Disease Control and Prevention. All the procedures followed the ethical review of animal experimentation welfare (No. 2020014).

Mice

C57BL/6J male mice aged 6 to 8 weeks were purchased from Beijing Vital River Laboratory Animal Technology Co., Ltd. CCR2-DTR-GFP mice were generated by Shanghai Model Organisms. *Sftpc-CreER; Rosa26*-mTmG and *Pdgfra*-eGFP mice were kindly provided by Prof. Nan Tang (National Institute of Biological Sciences, Beijing, China). All the mice were housed in the SPF environment.

Virus

The H1N1 (A/California/07/2009) virus was amplified in the Madin-Darby Canine Kidney (MDCK) cell Line. In brief, the MDCK cell Line at 100% confluence was washed twice with PBS, and then, the virus in DMEM was incubated on the cell surface for 1 h. After washing, the cells were incubated with DMEM supplemented with 1 μg/mL TPCK-Trypsin. The virus was collected when it showed a 70% cytopathic effect and stored at −80 °C. The virus titer was determined via plaque assay.

In vivo infection and treatment protocols

The influenza virus infection assay was performed in the ABSL2 animal laboratory center of the CDC after one week of acclimatization. Briefly, male and female mice were anesthetized with 250 mg/kg tribromoethanol via intraperitoneal injection, and then 20 PFU of H1N1 influenza virus in 50 μL of serum-free DMEM was administered intranasally to the mice. Body weight was monitored every 2–3 day, and the mice were considered dead when the body weight was less than 70% of the original weight.

For the deletion of Mo-Macs, CCR2-DTR-GFP mice were treated with Diphtheria toxin (DT). Briefly, DT (#D0546-1 mg, Sigma) was dissolved in 1 mL of ddH_2O. The 1 mg/mL stock solution was distributed in aliquots and stored at −80 °C. The DT was thawed at room temperature and diluted in DPBS at a 1:1000 ratio prior to use. The dosage for the mice was 10 ng/g, which was calculated on the basis of their body weight. Thus, a 20 g mouse was i.p. injected with 200 μL of 1 ng/μL DT.

Immunofluorescence staining

Mouse lung tissue was fixed with 4% PFA at 4 °C for 24 h by intratracheally injecting PFA into the lungs. The lung tissue was washed with PBS 3 times, dehydrated with 30% sucrose solution, and embedded in optimal cutting temperature (OCT) compound. For paraffin embedding, the lung tissue was dehydrated with gradient ethanol concentrations ranging from 70 to 100%, permeabilized with xylene, and then embedded in paraffin. The tissues were sliced to a thickness of 5–20 μm. The OCT-embedded slices were washed with PBS 3 times for immunofluorescence staining, while the paraffin-embedded slices were rehydrated with xylene and gradient ethanol from 100 to 70% and water. After that, antigen retrieval was conducted in sodium citrate buffer, nonspecific binding blockade and cell permeabilization were performed in 3% BSA with 1.5% Triton X-100. The primary antibodies were diluted in 3% BSA with 1.5% Triton X-100 and incubated at 4 °C overnight. After being washed with PBST 3 times, the secondary antibodies were diluted in BSA buffer and incubated at room temperature for 3 h, and DAPI was used for nuclear staining.

EdU staining was performed using the Click-iT EdU Imaging Kit (#C10337, Invitrogen). For the staining of mouse tissue, the mice were injected i.p. with 10 mg/mL EdU 2 h before sample collection. EdU staining was conducted following the instruction manual. H&E staining was conducted according to the manufacturer's instructions. The antibodies used for immunofluorescence staining are listed in Table S1.

Imaging

Histological images, such as H&E staining and whole-lung images, were taken with VS120. A zoomed-in image showing detailed information was taken with confocal microscopes such as Nikon A1, Nikon AX, or Zeiss800. Lung tissue (1 mm^3) from the injury site was fixed with glutaraldehyde fixation solution, embedded, and sectioned for EM imaging. The ultra-structures were examined with a Thermo Fisher Tecnai spirit G2 transmission electron microscope.

Flow cytometry analysis of immune cells

Mouse lung tissue was enzymatically digested into single cells. Briefly, mouse lung tissue was cut into 1 mm^3 fragments, digested in 5 mg/mL collagenase I and 0.5 mg/mL DNase I in 5 mL of HBSS in a 37 °C water bath for 45 min after cardiac perfusion, passed through 70 μm and 40 μm cell strainers, and then the red blood cells were lysed with lysis buffer (#R1010, Solarbio) at room temperature for 3 minutes. Single cells were resuspended in 1 mL of cell stain buffer, and the cell number was recorded. After that, the cells were stained with CD16/32 to block nonspecific binding and other specific cell markers for flow cytometry analysis. For the analysis of macrophages, fluorescent dye-conjugated secondary antibodies, including FITC-conjugated anti-mouse CD45, PE-conjugated anti-mouse CD64, APC-conjugated anti-mouse MerTK, PE-Cy7-conjugated anti-mouse CD11b and PerCP-Cy5.5-conjugated anti-mouse SiglecF, were used. The antibodies used for flow cytometry are listed in Table S2.

Magnetic cell separation (MACS) and scRNA-seq

Mouse lung tissue was enzymatically digested into single cells as described above. Single cells were resuspended in 270 μL of MACS buffer, incubated with 30 μL of CD31 beads (#130-097-418, Miltenyi) at 4 °C for 15 min, washed with 5 mL of MACS buffer and resuspended in 500 μL of MACS buffer. LD columns (#130-042-091, Miltenyi) were rinsed with MACS buffer and placed on a MidiMACS separator (#130-042-302, Miltenyi). The sample was added to the columns, and the $CD31^-$ cells were removed and collected in tubes. The sample was subsequently washed with 1 mL of MACS buffer 3 times. The samples at the indicated time points were mixed with 3 individuals. $CD31^-$ cells were processed via the standard protocol for scRNA-seq on the 10x Genomics platform, which was performed by *Genodenovo*. In brief, trypan blue was used to determine the cell number and survival rate. Gel beads with barcodes mixed with cell suspensions and enzymes formed the GEMs (gel beads in emulsions). Then, barcoded cDNA was generated via reverse transcription and amplified for efficient Library construction. cDNA was enzymatically cut into 200–300 bp segments, followed by end repair, a-tailing, and adaptor ligation; then, the DNA library was generated via PCR amplification. Finally, high-throughput sequencing of the DNA library was conducted on the Illumina sequencing platform PE150.

scRNA-seq data analysis

The raw data were converted to FASTQ files via 10x Genomics Cell Ranger. Reads were mapped to the reference genome (Mouse mm10) after the reads with low-quality barcodes and UMI were filtered out. Gene expression quantification was performed after the sequencing errors were corrected on the basis of the UMI sequence. The cell-by-gene matrices were imported into Seurat for downstream analysis. The expression quality control should be performed by filtering out unwanted cells with high mitochondrial gene percentages, high UMIs, and genes with fewer than 200 or more than 6000 copies. To minimize the effects of batch effects and behavioral conditions on clustering, we employed CCA, a method that first conducts canonical correspondence analysis (CCA) across all samples, then identifies mutual nearest neighbors (MNN) among cells to establish intercellular correspondences, and ultimately utilizes these correspondences as anchors to achieve data integration and batch effect correction. The CCA approach takes as input sample data following the removal of low-quality cells and yields a batch-corrected integrated dataset. After normalizing the data and batch effect correction, PCA was performed for dimensional reduction; then, the cells were clustered and visualized via t-distributed stochastic neighbor embedding (t-SNE). The cell types were annotated on the basis of their specific cell markers. Differentially expressed genes of one cluster compared with the rest of the cells were identified by $Log_2FC > 1$ and q value < = 0.05. GO and KEGG analyses were based on the Metascape database [21].

Mouse alveolar organoid culture

For the AT2 and fibroblast coculture assay, AT2 cells were isolated from *Sftpc-CreER*; *Rosa26*-mTmG mice after 4 tamoxifen treatments, and the mouse lungs were enzymatically digested into single cells with 35.2 mg of neutral protease (#NPRO2, Worthington) and 1 mg of DNase I in 5 mL of HBSS for 45 min in a 37 °C water bath. GFP^+ AT2 cells were isolated via flow cytometry. Fibroblasts were isolated from Pdgfra-eGFP mice. The lung tissue was digested with 35.2 mg of neutral protease (#NPRO2, Worthington), 4.5 mg of elastase (#2294, Worthington), 3.51 mg of collagenase I and 1 mg of DNase I in 5 mL of HBSS for 45 min in a 37 °C water bath. AT2 cells (1×10^4) with fibroblasts (2×10^5) were resuspended in 50 μL of culture medium, mixed with an equal volume of Matrigel (#345231, Corning) and cultured in transwells for 14 days. The culture medium was composed of 10% FBS, 1% P/S, 1× ITS, cholera toxin (#C8052, Sigma), epidermal growth factor (#PMG8044, Gibco), keratinocyte growth factor (#PHG0094, Gibco), hepatocyte growth factor (#PHG0324, Gibco), and fibroblast growth factor-basic (#PMG0034, Gibco) in DMEM-F12. Rock inhibitor (#C9903, Sigma) was added during the first 4 days. For the OSM in vitro stimulation assay, 50 pg/mL OSM protein (#495-MO-025, R&D Systems) was added to the culture medium from the initial day to 14 days.

For the AT2 and macrophage coculture assay, AT2 cells were isolated from C57BL/6J mice on the basis

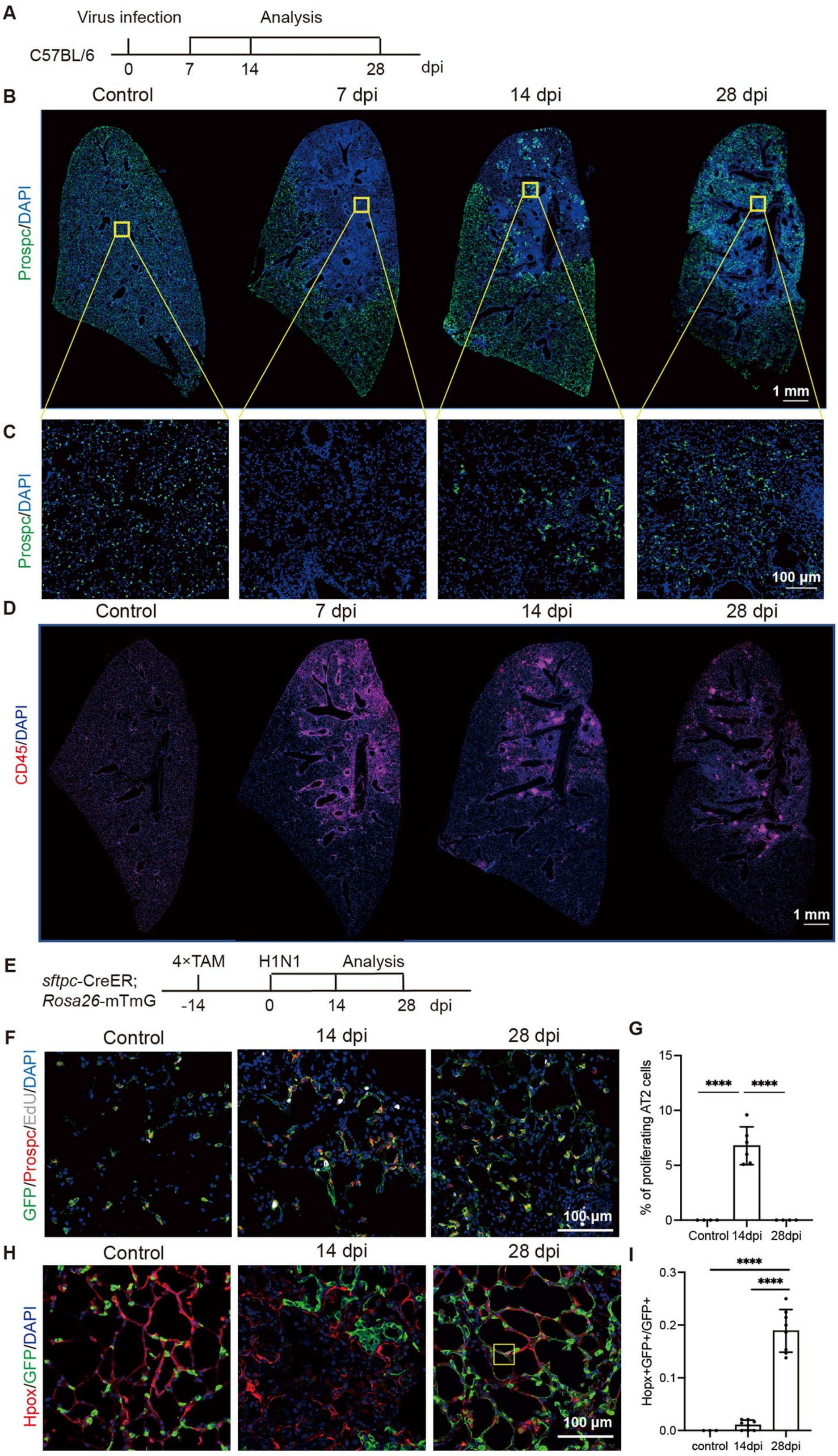

Fig. 1 (See legend on next page.)

(See figure on previous page.)

Fig. 1 Characterization of AT2 cells and immune cells during the recovery stage following H1N1 infection. (**A**) Flowchart illustrating the process of virus infection and sample collection in C57BL/6 mice. The influenza virus was intranasally infected into C57BL/6 mice, and lung tissues were collected and analyzed at 7, 14, and 28 dpi. dpi: days post infection. (n > = 3 for each time points) (**B**) The dynamic changes in and tissue distribution of AT2 cells in the injury and recovery states were analyzed by immunofluorescence staining. AT2 cells were stained with Prospc. (n > = 3 for each time point, representative pictures were shown here) (**C**) Enlarged confocal images of panel B. (**D**) Whole-lung images showing the dynamic changes in and tissue distribution of immune cells during injury and recovery, which were analyzed via immunofluorescence staining. CD45 was used to detect total immune cells. (**E**) Flowchart of H1N1-infected AT2 cell lineage tracing mice (*Sftpc-CreER*; *Rosa26*-mTmG). The mice were treated with tamoxifen 4 times beginning 14 days before H1N1 infection. Lung samples were collected and analyzed at 14 and 28 dpi. (**F**) AT2 cell proliferation at the injury site was determined by immunofluorescence staining. GFP represents the AT2 cell lineage, Prospc labels AT2 cells, and EdU represents proliferating cells. (**G**) Quantification of AT2 cell proliferation shown in panel **F**. (**H**) AT2 cell differentiation at the injury site was determined by immunofluorescence staining. Hopx labels AT1 cells. The right panels show enlarged images at 28 dpi. (**I**) Quantifications of AT2 cell differentiation shown in panel **H**. Data are presented as mean with SD. One-way ANOVA with post-hoc Tukey test was used for the statistical analysis (**G** and **I**). Scale bars: 1 mm (**B** and **D**) and 100 μm (**C**, **F** and **H**)

of previous reports [22]. Briefly, single lung cells were stained for CD326 (#118210, Biolegend), CD45 (#103115, Biolegend) and CD104 (#14-0161-82, Biolegend). $CD45^{-}CD326^{+}CD104^{-}$ cells were isolated via FACS. Mo-Macs were isolated from the lung tissue after influenza infection at 15 dpi and AMs were isolated from the lung tissue of the mock control. AT2 cells (1×10^4) were co-cultured with Mo-Macs or AMs (3×10^5) or cultured alone for 14 days. The culture medium was used as previously described [22–24]. Moreover, 20 μg/mL GM-CSF (#315−03, Peprotech) was added to maintain macrophage growth. Each group contained 3 replicates.

For the SC144 treatment on the AT2 and macrophage coculture assay. The culture medium with GM-CSF was supplemented with or without 0.1 μm Sc144 (#S7124, Selleck). Each group contained 3 replicates, and 2 independent experiments were performed.

To quantify the clone formation efficiency (CFE), the ratio of the number of alveolar spheres to the initial number of seeded AT2 cells was calculated. Especially, the alveolar spheres with a spherical shape structure and with a diameter larger than 0.15 mm were used for quantifications. For the quantifications of alveolar sphere size, the diameter larger than 0.54 mm was defined as large, larger than 0.27 mm which less than 0.54 mm was defined as medium, and smaller than 0.27 mm as small.

OSM stimulated AT2 cells in 2D in vitro culture

AT2 cells were isolated as described above [22]. The round coverslips were coated with 1% Matrigel at 37 °C for 1 h and washed with warm PBS. Isolated primary mouse AT2 cells were seeded onto round coverslips at a density of 2×10^4 per well in 24-well plates. AT2 cells were cultured on coverslips with DMEM-F12 supplemented with 1% P/S for 24 h, and OSM at the indicated concentration in DMEM-F12 was added for stimulation. The sample was collected 24 h after OSM stimulation.

Enzyme-linked immunosorbent assay (ELISA)

Serum was collected from whole blood by centrifugation at 25,000 rpm for 20 min after allowing the blood to clot for 30 min. Lung tissue was collected and homogenized in 1 mL of cold PBS and centrifuged at 5000 × g for 5 min, after which the supernatant was collected. The serum and lung supernatants were aliquoted and stored at −80 °C. The OSM protein concentration was tested via an OSM kit (#MSM00, RnD systems). All the measurements were performed following the standard protocol of the kit. The standard curve was generated on the basis of 4-PL.

Statistics

The data are shown in bar graphs. The means ± SDs or means ± SEMs per group are indicated by bars and error bars. Normality was tested before choosing the statistical methods. Student's t tests were used to compare two groups. For the analysis of three or more groups, we used ANOVA followed by Tukey's post hoc test. The significance level is denoted as ns (not significant, $P > 0.05$), * ($P < 0.05$), ** ($P < 0.01$), *** ($P < 0.001$), and **** ($P < 0.0001$). Graphs were prepared via GraphPad Prism (GraphPad Software version 10.1.1).

Results

Residual AT2 cells serve as the main alveolar stem cells in an inflammatory niche during severe H1N1 infection

The process of lung pathology after virus infection can be divided into four major stages: the homeostatic stage, the exudative phase, the proliferative phase, and the fibrosis phase [25, 26]. Delayed re-epithelialization can lead to lung fibrosis. To characterize the progression of H1N1-induced lung injury in a mouse model, we monitored the body weights of H1N1-infected mice for up to 28 days post infection (dpi). Lung samples were collected at 7, 14, and 28 dpi to assess tissue pathology comprehensively across different time points (Fig. 1A). The observed body weight changes indicated the peak injury phase at 8–10 dpi, followed by gradual recovery (Supplementary Fig. 1 A).

Alveolar epithelial cells, including AT2 cells, can be targeted by the H1N1 virus [27]. Immunofluorescence staining was performed to characterize the dynamic changes in AT2 cells from the injury stage to the recovery stage. Whole-lung images and zoomed-in images revealed that

H1N1 infection caused severe AT2 cell death at 7 dpi. At 14 dpi, aggregated AT2 cell clusters were observed in the damaged region, with a more decentralized distribution at 28 dpi (Fig. 1B-C). The number of AT2 cells in the injured region strongly decreased at 7 dpi, followed by a gradual increase from 14 to 28 dpi (Supplementary Fig. 1B). Concurrently, CD45$^+$ immune cells migrated from the parabronchial region to the alveolar region and remained in the damaged region during the recovery process, as shown by the specific CD45 staining and pathological H&E staining (Fig. 1D, Supplementary Fig. 1 C).

AT2 cells function as the stem cells of the alveoli [28, 29]. Given that the H1N1 influenza virus targets and induces AT2 cell death, understanding the mechanisms of AT2 cell regeneration following infection is essential. To investigate this process, we utilized AT2 lineage-tracing mice (*Sftpc-CreER*; *Rosa26*-mTmG), in which residual AT2 cells and their progeny were labeled with green fluorescence protein (GFP) (Fig. 1E). Immunofluorescence staining of Prospc and GFP revealed that 95% of newborn AT2 cells can be traced by GFP in the damaged region at 14 dpi (Supplementary Fig. 1D-E), which indicates that AT2 cells are the main stem cells in the alveoli in response to influenza virus infection. These findings align with recent studies suggesting that AT2 regeneration may involve alternative progenitor pools, such as club cells or bronchioalveolar stem cells (BASCs) [30]. Notably, while club cells (marked by *Scgb1a1*) and BASCs (co-expressing *Scgb1a1* and *Sftpc*) exhibit plasticity during injury, our lineage-tracing data indicate that AT2 cells predominantly self-renew under acute influenza infection, with limited contributions from heterologous progenitors.

Moreover, EdU staining, which labels proliferating cells, revealed that approximately 5% of AT2 cells in the damaged region exhibited high proliferative activity at 14 dpi (Fig. 1F-G, Supplementary Fig. 1 F). Additionally, confocal microscopy revealed that AT2 cells differentiated into type I alveolar epithelial (AT1) cells, as evidenced by the presence of GFP-labeled Hopx$^+$ AT1 cells at 28 dpi (Fig. 1H-I, Supplementary Fig. 1G). Cryo-electron microscopy revealed that AT2 cells started to colonize at 14 dpi, elongate, and secrete surfactant at 28 dpi (Supplementary Fig. 1H).

In summary, virus infection causes significant damage to the alveolar epithelial barrier. During recovery, residual AT2 cells proliferate and differentiate into AT1 cells, facilitating the repair and restoration of the alveolar barrier. In addition, this process is accompanied by immune cell infiltration (Supplementary Fig. 1I).

Transcriptional profiling of AT2 cells and infiltrating immune cells during H1N1-induced acute lung injury and recovery

To explore the responses of AT2 cells and infiltrating immune cells at the transcriptional level and identify specific cell subsets involved in lung regeneration, scRNA-seq was conducted on lung tissues from H1N1-infected mice at 10 and 21 dpi alongside mock-treated controls (Fig. 2A). The sequencing data were aligned to the mouse genome, and the cell subpopulations were identified and visualized via t-distributed stochastic neighbor embedding (t-SNE) (Fig. 2A-B). After multiple filtering, there were 16,164 cells in the control group, 17,214 cells in the 10 dpi group, and 12,790 cells in the 21dpi group. Subpopulation annotation was achieved on the basis of cell-specific markers (Supplementary Fig. 2 A). The results revealed a marked increase in T cells and macrophages, coupled with a reduction in AT2 cells, in response to H1N1-induced acute lung injury (Fig. 2C-D).

To characterize the transcriptional changes in AT2 cells, specifically expressed genes at each time point were calculated and visualized via a heatmap (Fig. 2E). Gene Ontology (GO) analysis of the differentially expressed genes revealed enrichment of Lipid metabolism processes in the homeostatic stage, with activation of antigen processing and presentation, viral genome replication inhibition, and cell adhesion and growth factor response at 10 dpi. The antigen processing and presentation of the peptide antigen process persisted at 21 dpi (Fig. 2F). These findings suggest that AT2 cells exhibit wound-healing functions during the recovery stage.

As mentioned above, T-cell and macrophage infiltration significantly increased in the lungs following H1N1 infection. To determine the function of those infiltrated T cells. T cells were unbiasedly re-clustered into eight distinct subsets (Supplementary Fig. 2B), with subsets identified on the basis of specific gene expression (Supplementary Fig. 2C, G). Cluster 7 is enriched in genes associated with mitochondria-associated genes. The specific marker genes of cluster 0–6 are listed (Supplementary Fig. 2G). T cells exhibit features such as an interferon response, migration, proliferation, cytotoxicity, and extracellular matrix synthesis. Quantifications of the dynamic changes in T-cell subsets revealed that interferon-responsive T cells, migrating T cells, proliferating T cells, and activated T-cell subsets were highly enriched post-H1N1 infection (Supplementary Fig. 2H). GO analysis of the activated T cells indicated that the granzyme-mediated programmed cell death process was enriched (Supplementary Fig. 2I). Histological and immunofluorescence staining confirmed T-cell infiltration and proliferation in the alveoli (Supplementary Fig. 2D-F). In conclusion, T cells displayed cytotoxic functions at the transcriptional level.

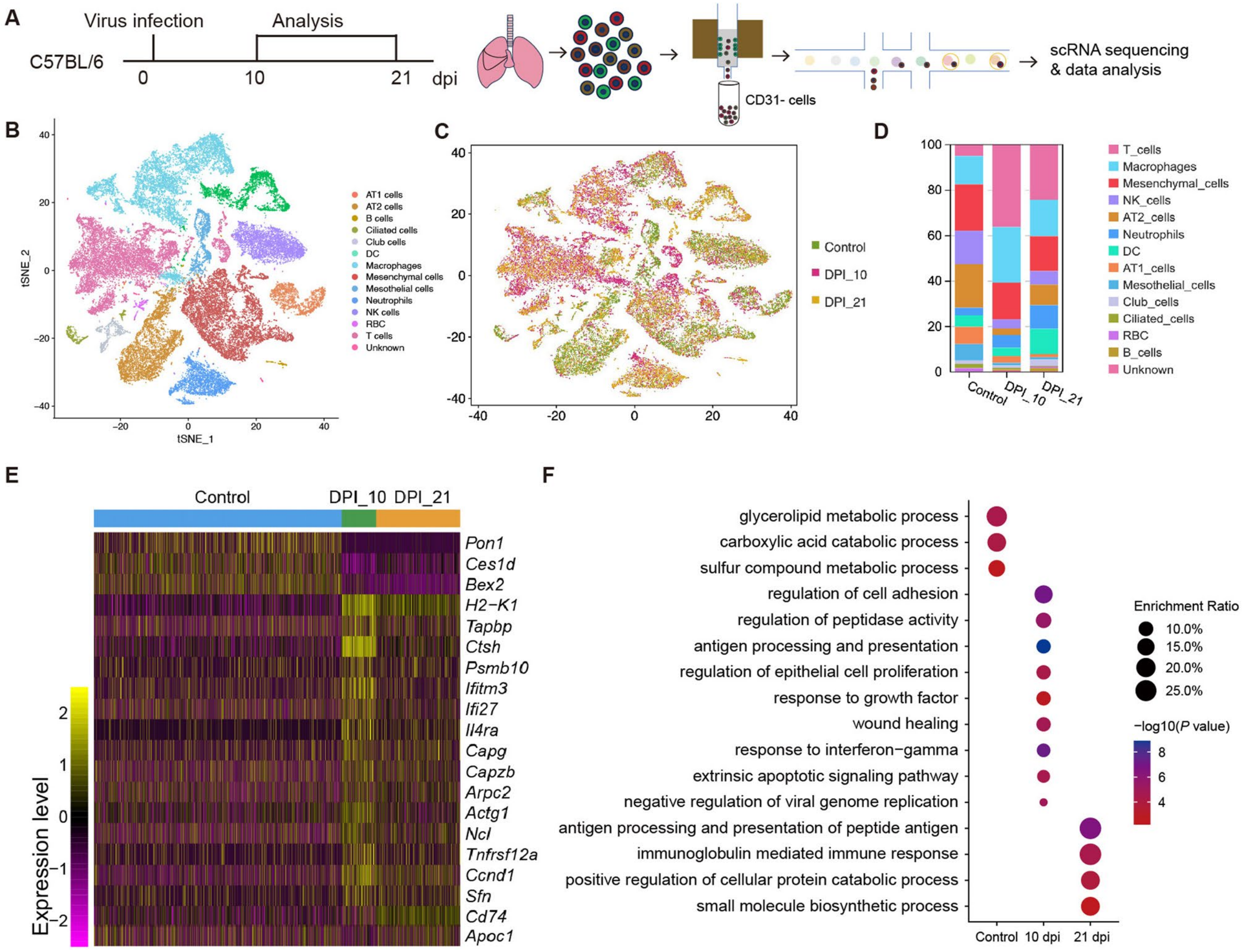

Fig. 2 Transcriptional features of AT2 cells and T cells in the recovery phase revealed by scRNA-seq. **A** Schematic diagram showing the process of scRNA-seq. Lung samples from H1N1-infected mice at the indicated time points were collected and enzymatically digested into single cells. CD31$^-$ cells were sorted after bead incubation and magnetic-activated cell sorting (MACS), and CD31$^-$ cells were processed according to the 10× Genomics protocol for sequencing and data analysis. Each time point contained 3 mice for replication. **B** Total cells were dimensionally reduced and visualized via t-SNE and then annotated on the basis of specific markers. **C** The distribution of each cell type at the indicated time points via t-SNE. **D** Quantification of the percentage of each cell type at the indicated time points, as shown in Fig. 2B-C. **E** Heatmap showing the highly expressed typical genes in AT2 cells at each time point. **F** Dot plot showing the GO features of AT2 cells at each time point according to the genes specifically expressed, as shown in Fig. 2E. The color indicates the -log $_{10}$ (*P* value), and the dot size indicates the enrichment ratio

Mo-Macs are spatially localized within regenerative foci and are characterized by the transcriptional regulation of epithelial cell proliferation

The number of macrophages significantly increased following H1N1 infection, as revealed by the aforementioned scRNA-seq analysis. To study the characteristics of the macrophage subsets and their specific functions, the macrophages were clustered into 4 distinct subsets (Fig. 3A). On the basis of the expression profiles of the marker genes previously reported [31], these subsets were designated monocytes, monocyte-derived macrophages (Mo-Macs), proliferating macrophages and alveolar macrophages (AMs) (Fig. 3B). Further functional analysis, including GO enrichment analysis of specifically expressed genes, revealed that monocytes were enriched for pathways related to monocyte extravasation, Mo-Macs for the inflammatory response and regulation of epithelial cell proliferation, AMs for lipid metabolism pathways, and proliferating macrophages for DNA replication processes (Fig. 3C). Additionally, temporal analysis revealed a marked increase in Mo-Macs and a concurrent decrease in AMs following H1N1 infection (Fig. 3A). To validate these findings, flow cytometry analysis of AMs and Mo-Macs was conducted on H1N1-infected lung tissue at the indicated time points (Supplementary Fig. 3A-C). These results were consistent with the scRNA-seq data, which revealed a decrease in AMs and an increase in Mo-Macs after infection (Fig. 3D and E).

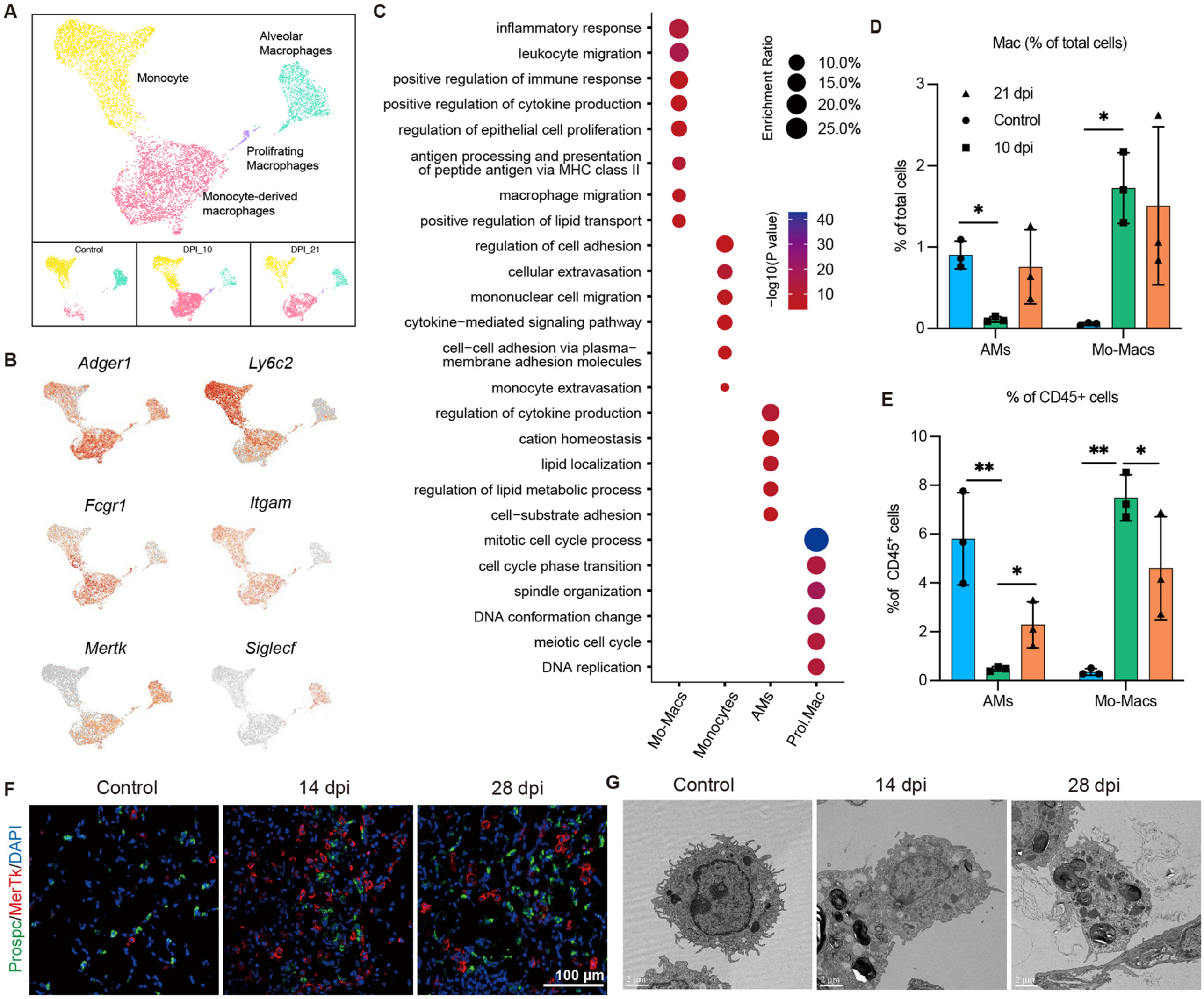

Fig. 3 Tanscriptomic and spactial data suggest a potential role of infiltrated Mo-Macs in epthelial cell regeneration. **A** Monocytes and macrophages were reclustered into 4 subsets (top panel), and their distributions were determined at the indicated time points (bottom panel). **B** Expression of selected genes in reclustered monocytes and macrophages. A darker color indicates higher expression. **C** Dot plot showing the GO characteristics of the genes specifically expressed in each cell type. Mo-Macs: Monocyte-derived macrophages; AMs: Alveolar macrophages; Prol. Mac: Proliferating macrophages. **D** Quantification of the percentages of AMs and Mo-Macs among total cells at the indicated time points. **E** Quantification of the percentages of AMs and Mo-Macs among $CD45^+$ immune cells at the indicated time points. **F** Confocal images showing the spatial relationship between macrophages and AT2 cells. MerTK (red) labels macrophages, while Prospc (green) labels AT2 cells. **G** The ultrastructures of macrophages at the indicated time points and their spatial correlations with AT2 cells at 14 dpi. Data are presented as mean with SD, $n=3$ for each group (**D**-**E**). One-way ANOVA with post hoc Turkey test was used for the statistical analysis. 3 samples at the injury site for each group were chosen for the slicing and analysis (**G**). Scale bars: 100 μm (**F**)

To further explore the spatial distributions of macrophages during the regenerative process, immunofluorescence staining and confocal microscopy were conducted. The results revealed that $MerTK^+$ macrophages were in close proximity to AT2 cells within the regenerative regions (Fig. 3F). Additionally, cryo-electron microscopy revealed that macrophages closely interact with AT2 cells at the early stages of regeneration and subsequently phagocytose surfactant material at the late stages (Fig. 3G).

Collectively, these data suggest that highly infiltrated Mo-Macs are characterized by the regulation of epithelial cell proliferation at the transcriptional level and are spatially located within regenerative foci, a distribution pattern that may promote alveolar regeneration following H1N1 infection.

Mo-Macs promote alveolar epithelial regeneration in vitro and in vivo

To investigate the effect of Mo-Macs on alveolar epithelial regeneration, an AT2 and macrophage coculture system was utilized. Primary Mo-Macs were isolated from the lungs of H1N1-infected mice at 14 dpi, whereas AMs were isolated from the lungs of mock-infected mice. Compared with AT2 cells cultured alone, AT2 cells cocultured with either Mo-Macs or AMs significantly enhanced the formation of alveolar organoids (Fig. 4A and B). The effect was pronounced in large-, medium- and small-sized organoids (Supplementary Fig. 4 A).

To further determine the regulatory function of Mo-Macs in vivo, transgenic CCR2-DTR-GFP mice were generated for in vivo cell depletion. As previous studies reported, the migration of monocytes to injured lung tissue is mediated by the CCL2-CCR2 signaling pathway. Inducible depletion of CCR2$^+$ cells, mainly Mo-Macs, is achieved via the diphtheria toxin/diphtheria toxin receptor (DT/DTR) system. The efficiency of DT was assessed by evaluating the proportion of GFP$^+$ cells in the bone marrow and lung, as well as the number of AMs and Mo-Macs in the lungs. DT treatment significantly reduced the percentage of GFP$^+$ cells and markedly decreased the number of AMs and Mo-Macs in the lungs of H1N1-infected mice at 21 dpi (Supplementary Fig. 4E-H).

To explore the function of Mo-Macs, DTs were first injected from 8 dpi until the days of sampling (Supplementary Fig. 4B). Survival rates and body weight changes were evaluated. The data revealed that DT treatment reduced the ratio of death, although the difference was not significant (Supplementary Fig. 4 C), suggesting the inflammatory function of Mo-Macs. However, body weight analysis revealed that DT treatment delayed the recovery of H1N1-infected mice (Supplementary Fig. 4D). To further elucidate the effects of Mo-Macs at the recovery stage, DTs were injected beginning at 13 dpi, which is a time point at which body weight typically begins to recover (Fig. 4C). Quantification of the GFP$^+$ cells in the bone marrow revealed that the GFP$^+$ cells were successfully depleted (Fig. 4E). Consistent with earlier findings, DT treatment resulted in delayed body weight recovery (Fig. 4D). Histopathological examination at 21 dpi revealed that DT-mediated depletion of Mo-Macs led to significant accumulation of cellular debris in the alveolar lumen and disrupted the lung structure (Fig. 4F). Immunofluorescence staining of AT1 and AT2 cells further revealed abnormal alveolar structures in the DT-treated group (Fig. 4G-H). MerTK staining confirmed successful depletion of macrophages in the alveolar lumen in the DT-treated group at 21 dpi (Fig. 4I-J).

In conclusion, our study elucidated the role of Mo-Macs in promoting AT2 cell activity through an in vitro coculture system and demonstrated that the depletion of Mo-Macs leads to impaired alveolar regeneration.

The OSM-OSMR signaling pathway mediates macrophage-driven AT2 cell regeneration postinfection

To identify the potential mediators by which macrophages promote AT2 regeneration, bioinformatic analysis of cell−cell interactions, which is based on ligand−receptor pairs, between Mo-Macs and AT2 cells at 10 dpi was conducted. AT2 cells secrete autocrine signals such as FGF1 and BMP4/5, which are known to promote AT2 cell proliferation [6]. Additionally, AT2 cells expressing GAS6 interact with MerTK and Axl on Mo-Macs, facilitating the phagocytosis of dying cells [32, 33]. Moreover, Mo-Macs secrete factors such as OSM, which bind to its receptors OSMR and IL6st on AT2 cells (Fig. 5A).

Previous studies have reported that OSM, a member of the IL6 cytokine family, is secreted by lymphatic cells and monocytes and is involved in inflammatory and tissue repair processes, including those associated with virus infections, cardiac fibrosis, and asthma [34–37]. However, the regulatory role of OSM in alveolar regeneration after lung injury remains unclear. To address this, we first analyzed the expression pattern of the OSM-IL6st/OSMR signaling pathway following H1N1 infection, focusing on the cell types expressing these genes and their dynamic changes at both the transcriptional and protein levels. scRNA-seq analysis revealed that *Osm* is expressed primarily in macrophages and neutrophils, *Osmr* is expressed in AT2 cells and fibroblasts, and *Il6st* is broadly expressed across most cell types, including AT2 cells (Fig. 5B). Postinfection transcriptional analysis revealed an increase in *Osm* in macrophages and *Osmr* in AT2 cells at 10 dpi, whereas *Il6st* expression remained unchanged (Fig. 5C). Similarly, in vitro experiments of AT2 organoids infected with H1N1 confirmed elevated *Osmr* expression and no significant changes in *Il6st* expression (Supplementary Fig. 5 A, B). Additionally, we measured OSM protein dynamics in lung tissue and serum via ELISA. The results demonstrated that the OSM levels in the lung tissue increased significantly from 3 dpi to 14 dpi (Fig. 5D), whereas the OSM level was below the lower limit of detection in the serum (Supplementary Fig. 5 C).

To explore the biological function of OSM in AT2 cells, we applied recombinant mouse OSM to the AT2 sphere culture system. The in vitro sphere culture results revealed that OSM increased the number and size of alveolar spheres (Fig. 5E and F), suggesting a potential role in enhancing AT2 cell activity under those culture conditions. Previous studies have indicated that OSM exerts its functions through activation of the downstream JAK-STAT3 signaling pathway [34]. In vitro cell culture data confirmed that OSM treatment stimulated p-STAT3 nuclear translocation in AT2 cells (Fig. 5G), which proves that OSM also activated STAT3 signaling in AT2 cells. Additionally, p-STAT3 translocation was observed in

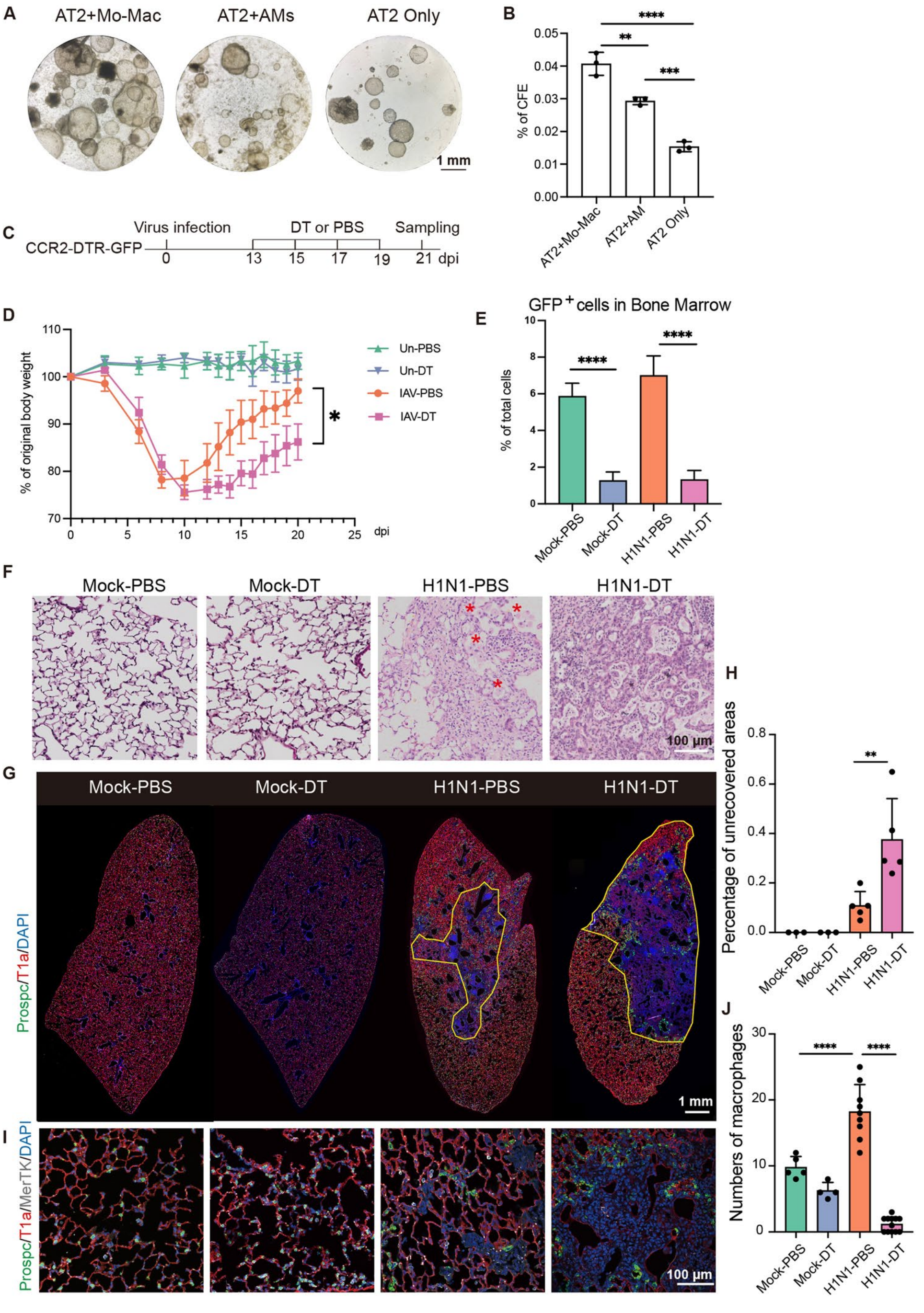

Fig. 4 Mo-Macs promoted alveolar repair in vitro and in vivo. (**A**) Bright-field images of AT2 spheres cocultured with Mo-Macs or AMs or cultured alone. **B** Quantification of the colony formation efficiency (CFE) of AT2 cells in each group. **C** Schematic diagram showing the process of virus infection, DT-mediated cell depletion, and lung harvesting in CCR2-DTR-GFP mice. DTs were treated from 13 dpi to 19 dpi, and lung samples were collected at 21 dpi. **D** Changes in the body weight of each group. PBS or DT treatment of mock- or H1N1-infected mice. The data are presented as the means with SEMs. **E** Quantification of the ratio of GFP$^+$ cells in the bone marrow of each group. The data are presented as the means with SD. **F** The representative histological characteristics of each group are shown by H&E staining. Asterisks indicate macrophages in the PBS-treated H1N1 infection group. **G** The representative whole-lung images showing the alveolar epithelial barrier in each group. The yellow line indicates damaged areas. **H** Quantification of the damaged region, as shown in panel **G**. **I** Confocal images showing the degree of macrophage persistence in each group. MerTK (white) labels macrophages. **J** Quantification of the macrophage cell number, as shown in panel **I**. MOCK-PBS (*n* = 3); MOCK-DT (*n* = 3); H1N1-PBS (*n* = 5); H1N1-DT (*n* = 5); Data were pooled from two independent experiments. An unpaired t-test was utilized for statistics (**D**). Data are presented as mean with SD (**B**, **E**, **H** and **J**), mean with SEMs (**D**). One-way ANOVA with post-hoc Tukey test was used for the statistical analysis (**B**, **E**, **H**, and **J**). Scale bars: 1 mm (**A**), 100 μm (**F** and **H**), and 1 mm (**G**)

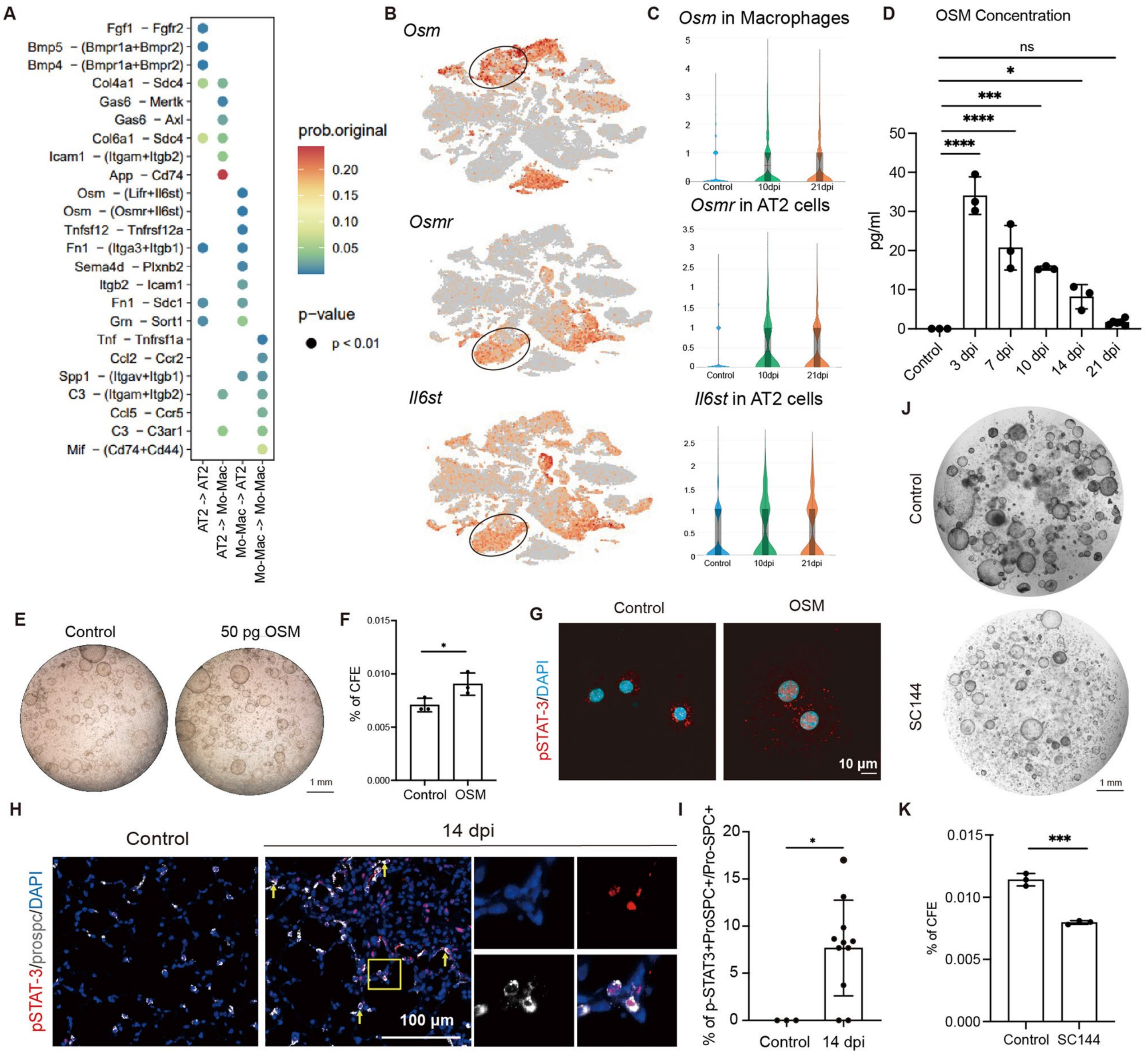

Fig. 5 OSM participated in the alveolar regeneration process. (**A**) Dot plot showing the cell-cell interactions between Mo-Macs and AT2 cells. The row names represent the ligand-receptor pairs, and the column names represent the mode of cell-cell interactions, e.g., AT2->Mo-Macs indicate AT2-derived factors acting on the receptors expressed on Mo-Macs. The color indicates the possibility of interaction. **B** The expression of *Osm*, *Osmr*, and *Il6st* in total cells. **C** Violin plot showing the expression of *Osm* in macrophages and *Osmr* and *Il6st* in AT2 cells in the control, 10 dpi, and 21 dpi groups. **D** Quantification of the OSM protein concentration in the lung supernatant at the indicated time points. **E** Bright-field image showing AT2 sphere colony formation with and without OSM treatment. Representative experiment based on 3 times independent replicates. **F** Quantification of the percentage of colony formation efficiency of each group, as shown in panel **E**. **G** Confocal images showing p-STAT3 activation in in vitro cultured AT2 cells post-OSM stimulation. **H** Confocal images showing p-STAT3 expression in mouse lung tissue at 14 dpi. **I** Quantifications of percentage of p-STAT3$^+$ ProSPC$^+$/ProSPC$^+$ cells, as shown in panel **H**. **J** Bright-field image showing AT2 sphere colony formation in AT2 and Mo-Macs co-culture system with and without SC144 treatment. Representative experiment based on two independent replicates. **K** Quantification of the percentage of colony formation efficiency of each group, as shown in panel **J**. Data are presented as mean with SD (**D**, **F**, **I**, and **K**), One-way ANOVA with post hoc Tukey test (**D**) and unpaired t-test was used for the statistical analysis (**F**, **I**, and **K**). Scale bars: 1 mm (**E** and **J**), 100 μm (**H**), and 10 μm (**G**)

AT2 cells at 14 dpi in vivo (Fig. 5H-I). Furthermore, to investigate whether the OSM-OSMR/IL6st signaling axis mediates the direct interaction between Mo-Macs and AT2 cells. We employed the Il6st inhibitor SC144 in an in-vitro co-culture system. Treatment with SC144 significantly reduced the formation of alveolar spheres, suggesting thay IL6st signaling is functionally required for AT2 cell activation in response to Mo-Macs-derived signals (Fig. 5J-K).

Taken together, these findings suggest that the OSM-OSMR/IL6st signaling pathway plays a key role in mediating the proliferative effects of Mo-Macs on AT2 cells. Post infection, the expression of OSM was elevated, and OSM promoted AT2 sphere formation in vitro, accompanied by the activation of p-STAT3. Moreover, pharmacological inhibition of OSM-OSMR/IL6st signaling in a Mo-Macs and AT2 cell co-culture system significantly suppressed the formation of alveolar spheres, further supporting a functional role for this pathway in promoting AT2 cell activity.

Discussion

Lung regeneration following acute injury, such as that induced by influenza virus infection, involves complex interactions between immune cells, epithelial cells, and inflammatory signals. Recent studies have emphasized the role of immune cells, including group 3 innate lymphoid cells and regulatory T cells, in promoting lung repair [7, 38, 39]. Additionally, monocytes, which migrate to the injury site and differentiate into monocyte-derived macrophages (Mo-Macs) following infection [15, 40], have been shown to exhibit dynamic changes in their population during influenza virus infection [16], providing a focal point for understanding the recovery process.

Emerging technologies, including scRNA-seq and unbiased analysis, confocal imaging, and transgenic mouse models, pave the way for the systemic characterization and exploration of the underlying mechanisms of the regeneration process. The systemic characterization of alveolar epithelial cell injury and the subsequent regeneration process indicate that alveolar epithelial regeneration involves an inflammatory niche and is mediated by the proliferation, migration, and differentiation of AT2 cells. To investigate the potential functional and transcriptional changes in alveolar epithelial cells and infiltrating immune cells at the recovery stage, scRNA-seq of the lungs of H1N1-infected mice was conducted. While we acknowledge that AT2 proliferation may peak at 14 dpi, we selected 10 dpi as the scRNA-seq time point to capture the initial phase of epithelial regeneration, as indicated by the weight recovery curves. The results revealed that AT2 cells exhibit several features, including negative regulation of virus replication, regulation of cell adhesion, and wound healing at the early recovery stage. Moreover, T cells and macrophages are highly enriched in the lung after virus infection. T cells infiltrate and proliferate in the injured lung, contributing to interferon response and cytotoxic effects. Moreover, we characterized a subset of T cells expressing extracellular matrix-associated genes. While the functional significance of those cells remains unclear, their gene expression profile raises the possibility that T cells may influence the extracellular matrix remodelling. This suggests a potential role not only in regeneration but also in pathological outcomes such as lung fibrosis, which can occur in parallel with aberrant repair, as reported in a previous study [27]. However, further in-depth studies are required to clarify the role of T cells in lung repair and their potential contribution to fibrosis.

Previous studies have suggested that Mo-Macs emigrate from the bone marrow via the CCL2-CCR2 signaling pathway [15, 41]. Notably, the mortality rate of CCR2$^{-/-}$ mice significantly decreased after H1N1 infection, indicating the pathological role of Mo-Macs [40]. Moreover, Mo-Macs exhibit proinflammatory features that determine the severe outcome of H1N1 infection [16]. Conversely, recent studies have proposed that Mo-Macs also play a role in the process of lung regeneration after sterile [17] or inflammatory injury [10]. These conflicting findings highlight the complexity of their role, with evidence indicating that the involvement of Mo-Macs in lung pathology and regeneration appears to depend on the timing of their activation and the context in which they function.

Our experiments using CCR2-DTR-GFP mice, which allow for the depletion of Mo-Macs at specific time points [42], reveal two critical insights. First, depletion of Mo-Macs at 8 days post infection (dpi) resulted in reduced mortality, indicating that Mo-Macs contribute to the severity of infection. Second, depleting Mo-Macs from 13 dpi delayed the recovery process, suggesting their indispensable role in facilitating lung regeneration at later stages. The transcriptional analysis of Mo-Macs and epithelial cells further confirmed the complexity of their roles. Mo-Macs exhibit features of both inflammation and epithelial regulation. These results support the hypothesis that Mo-Macs perform dual functions—promoting inflammation early in infection while facilitating tissue repair during the recovery phase. Although our findings suggest that Mo-Macs may undergo time-dependent functional reprogramming, systematic high-resolution analyses, such as time-series scRNA-seq or proteomic profiling, will be essential to validate this transition. Such approaches will not only clarify the underlying mechanisms but also resolve Mo-Mac subpopulations with distinct temporal roles, thereby providing a more comprehensive framework for therapeutic targeting. And we have to acknowledge that the CCR2-DTR-GFP model may affect other CCR2-expressing populations, including circulating monocytes. Further research is needed to explore the functions and underlying mechanisms of Mo-Macs to better understand and improve pathology and regeneration following H1N1 infection. There is an increased infiltration of inflammatory immune populations after Mo-Macs depletion in the lung, which we hypothesize to be neutrophils or T cells based on their morphology and distribution. Further characterization of these populations will be critical for uncovering additional mechanisms underlying delayed recovery.

To investigate the molecular mechanisms underlying the role of Mo-Macs in regeneration, we utilized cell−cell interaction analyses and identified OSM as a potential mediator. OSM, a member of the IL-6 cytokine family, is produced by activated T cells or monocytes and functions through the JAK-STAT1/3 or MAPK-Erk signaling pathway [34]. Functionally, OSM stimulates the proliferation of human lung fibroblasts [43], while OSMR overexpression exacerbates cardiac fibrosis [35]. Moreover, OSM is thought to be associated with severe asthma, and anti-OSM antibodies could be therapeutic targets for asthma [36, 37]. While OSM emerged as a prominent candidate in our study, we acknowledge that a broader analysis of macrophage-derived signaling in tissue regeneration will be essential for identifying additional mediators that contribute to lung regeneration.

In our study, OSM promoted alveolar organoid formation in vitro, and mechanistically, it activated STAT3 signaling in AT2 cells, reinforcing its role in epithelial repair. However, we also observed OSMR expression in fibroblasts, raising the intriguing possibility that OSM might simultaneously drive fibrotic processes via fibroblast activation during repair. This dual role of OSM—promoting epithelial regeneration while potentially contributing to fibrosis—highlights a critical research gap. Future studies should investigate whether OSMR$^+$ fibroblasts mediate fibrotic remodeling downstream of OSM signaling, particularly in chronic inflammatory contexts. Our study highlights the role of OSM in viral lung injury models, but its validation across other pathological contexts is necessary to establish broader relevance. Extending investigations to diverse disease models will help confirm conserved mechanisms, define the therapeutic window, and clarify potential limitations, thereby strengthening its translational potential and clinical applicability.

In summary, our findings offer a systemic characterization of the alveolar epithelial regeneration process following H1N1 infection, with particular emphasis on the pivotal role of Mo-Macs. By balancing their proinflammatory and pro-regenerative functions, Mo-Macs contribute to both the severity of the disease and the recovery process. These results suggest that further investigation into the specific mechanisms underlying Mo-Mac-mediated regeneration will be crucial for developing targeted therapeutic strategies to improve recovery outcomes in patients with acute lung injury. Additionally, understanding the role of cytokines such as OSM in this process could provide novel avenues for therapeutic intervention in lung fibrosis and other pulmonary diseases.

Data Availability

All the data are available from the corresponding author upon reasonable request. The raw scRNA-seq data will be uploaded to the Gene Expression Omnibus (GEO) repository.

Abbreviations

AT1	Alveolar Type Ⅰ cells
AT2	Alveolar Type Ⅱ cells
AM	Alveolar Macrophages
CCR2	CC-Motif Chemokine Receptor 2
DTR	Diphtheria Toxin Receptor
DPI	Days post infection
GFP	Green Fluorescent Protein
GO	Gene Ontology
HA	Hemagglutinin
IFN	Interferon
Mo-Macs	Monocyte-derived macrophages
Mono	Monocytes
OSM	Oncostatin-M
PCA	Principal Component Analysis
Proli	Proliferation
scRNA-seq	Single cell RNA sequencing
STAT3	Signal Transducer and Activator of Transcription 3

Supplementary Information

The online version contains supplementary material available at https://doi.org/10.1186/s12931-025-03359-7.

Supplementary Material 1.

Acknowledgements

We highly appreciate the valuable suggestions provided by Prof. Nan Tang at the National Institute of Biological Science, Beijing, and Prof. Xiaohuan Guo at Tsinghua University. We sincerely thank the staff of the Laboratory Animal Center of the Chinese Center for Disease Control and Prevention for their kind help with the animal experiments. We are grateful for the technical support provided by the flow cytometry facility, image center, and electron microscope center at the National Institute of Biological Science, Beijing. Additionally, we acknowledge Ennan Bin for performing the scRNA-seq data analysis and visualization.

Authors' contributions

Dr. Bin Cao and Dr. Hui Li proposed the concept and edited the manuscript. Xiao Shang performed the experiments and data analysis and wrote the original manuscript. Ju Jia, Jiapei Yu, Zeyi Wang, and Jiuyang Xu supported flow cytometry and edited the manuscript. Shumei Zou helped with the animal experiments.

Funding

This research was supported by funds from the National Natural Science Foundation of China (NSFC, NO.82030002/H0104, NO.82270010/H0102), the Beijing Nova Program of Science and Technology under grant NO.20220484049 and the National High Level Hospital Clinical Research Funding, the Elite Medical Professionals Project of China-Japan Friendship Hospital (No. ZRJY2021-QM09).

Data availability

No datasets were generated or analysed during the current study.

Declarations

Ethics approval and consent to participate

The animal study was approved and conducted in the ABSL-2 laboratory at the Chinese Center for Disease Control and Prevention Laboratory Animal Center.

Consent for publication
Not applicable.

Competing interests
The authors declare no competing interests.

Author details
[1]Department of Basic Medicine, Tsinghua University, Beijing 100084, China
[2]Department of Infectious Disease, Beijing Friendship Hospital, Capital Medical University, Beijing 100050, China
[3]Department of Pulmonary and Critical Care Medicine, Center of Respiratory Medicine, China-Japan Friendship Hospital, No.2 East Yinghua Road, Chaoyang District, Beijing 100029, China
[4]Institute of Respiratory Medicine, Chinese Academy of Medical Sciences and Peking Union Medical College, Beijing 100730, China
[5]National Institute for Viral Disease Control and Prevention, Collaborative Innovation Center for Diagnosis and Treatment of Infectious Diseases, Key Laboratory for Medical Virology, Chinese Center for Disease Control and Prevention, Beijing 102206, China

Received: 14 March 2025 / Accepted: 6 September 2025

References
1. Herold S, Becker C, Ridge KM, Budinger GR. Influenza virus-induced lung injury: pathogenesis and implications for treatment. Eur Respir J. 2015;45(5):1463–78.
2. Clementi N, Ghosh S, De Santis M, Castelli M, Criscuolo E, Zanoni I, Clementi M, Mancini N. Viral respiratory pathogens and lung injury. Clin Microbiol Rev. 2021;34(3) :e00103–20.
3. Uyeki TM, Hui DS, Zambon M, Wentworth DE, Monto AS. Influenza. Lancet. 2022;400(10353):693–706.
4. Bai L, Gu L, Cao B, Zhai XL, Lu M, Lu Y, Liang LR, Zhang L, Gao ZF, Huang KW, et al. Clinical features of pneumonia caused by 2009 influenza A(H1N1) virus in beijing, China. Chest. 2011;139(5):1156–64.
5. Zacharias WJ, Frank DB, Zepp JA, Morley MP, Alkhaleel FA, Kong J, Zhou S, Cantu E, Morrisey EE. Regeneration of the lung alveolus by an evolutionarily conserved epithelial progenitor. Nature. 2018;555(7695):251–5.
6. Juul NH, Stockman CA, Desai TJ. Niche cells and signals that regulate lung alveolar stem cells in vivo. Cold Spring Harb Perspect Biol. 2020;12(12):035717.
7. Monticelli LA, Sonnenberg GF, Abt MC, Alenghat T, Ziegler CG, Doering TA, Angelosanto JM, Laidlaw BJ, Yang CY, Sathaliyawala T, et al. Innate lymphoid cells promote lung-tissue homeostasis after infection with influenza virus. Nat Immunol. 2011;12(11):1045–54.
8. Liu Q, Dwyer GK, Zhao Y, Li H, Mathews LR, Chakka AB, Chandran UR, Demetris JA, Alcorn JF, Robinson KM et al. IL-33-mediated IL-13 secretion by ST2+Tregs controls inflammation after lung injury. JCI Insight. 2019; 4(6):e123919.
9. Mock JR, Dial CF, Tune MK, Gilmore RC, O'Neal WK, Dang H, Doerschuk CM. Impact of regulatory T cells on type 2 alveolar epithelial cell transcriptomes during resolution of acute lung injury and contributions of IFN-gamma. Am J Respir Cell Mol Biol. 2020;63(4):464–77.
10. Choi J, Park JE, Tsagkogeorga G, Yanagita M, Koo BK, Han N, Lee JH. Inflammatory signals induce AT2 Cell-Derived Damage-Associated transient progenitors that mediate alveolar regeneration. Cell Stem Cell. 2020;27(3):366–e382367.
11. Katsura H, Kobayashi Y, Tata PR, Hogan BLM. IL-1 and TNFalpha contribute to the inflammatory niche to enhance alveolar regeneration. Stem Cell Rep. 2019;12(4):657–66.
12. Broggi A, Ghosh S, Sposito B, Spreafico R, Balzarini F, Lo Cascio A, Clementi N, De Santis M, Mancini N, Granucci F, et al. Type III interferons disrupt the lung epithelial barrier upon viral recognition. Science. 2020;369(6504):706–12.
13. Major J, Crotta S, Llorian M, McCabe TM, Gad HH, Priestnall SL, Hartmann R, Wack A. Type I and III interferons disrupt lung epithelial repair during recovery from viral infection. Science. 2020;369(6504):712–7.
14. Wynn TA, Vannella KM. Macrophages in tissue repair, regeneration, and fibrosis. Immunity. 2016;44(3):450–62.
15. Serbina NV, Pamer EG. Monocyte emigration from bone marrow during bacterial infection requires signals mediated by chemokine receptor CCR2. Nat Immunol. 2006;7(3):311–7.
16. Li F, Piattini F, Pohlmeier L, Feng Q, Rehrauer H, Kopf M. Monocyte-derived alveolar macrophages autonomously determine severe outcome of respiratory viral infection. Sci Immunol. 2022;7(73):eabj5761.
17. Lechner AJ, Driver IH, Lee J, Conroy CM, Nagle A, Locksley RM, Rock JR. Recruited monocytes and type 2 immunity promote lung regeneration following pneumonectomy. Cell Stem Cell. 2017;21(1):120–e134127.
18. Misharin AV, Morales-Nebreda L, Reyfman PA, Cuda CM, Walter JM, McQuattie-Pimentel AC, Chen CI, Anekalla KR, Joshi N, Williams KJN, et al. Monocyte-derived alveolar macrophages drive lung fibrosis and persist in the lung over the life span. J Exp Med. 2017;214(8):2387–404.
19. Bailey JI, Puritz CH, Senkow KJ, Markov NS, Diaz E, Jonasson E, Yu Z, Swaminathan S, Lu Z, Fenske S et al. Profibrotic monocyte-derived alveolar macrophages are expanded in patients with persistent respiratory symptoms and radiographic abnormalities after COVID-19. Nat Immunol. 2024; 25(11):2097–2109.
20. Ruscitti C, Abinet J, Marechal P, Meunier M, de Meeus C, Vanneste D, Janssen P, Dourcy M, Thiry M, Bureau F, et al. Recruited atypical Ly6G(+) macrophages license alveolar regeneration after lung injury. Sci Immunol. 2024;9(98):eado1227.
21. Zhou Y, Zhou B, Pache L, Chang M, Khodabakhshi AH, Tanaseichuk O, Benner C, Chanda SK. Metascape provides a biologist-oriented resource for the analysis of systems-level datasets. Nat Commun. 2019;10(1):1523.
22. Weiner AI, Jackson SR, Zhao G, Quansah KK, Farshchian JN, Neupauer KM, Littauer EQ, Paris AJ, Liberti DC, Scott Worthen G, et al. Mesenchyme-free expansion and transplantation of adult alveolar progenitor cells: steps toward cell-based regenerative therapies. NPJ Regen Med. 2019;4:17.
23. Katsura H, Sontake V, Tata A, Kobayashi Y, Edwards CE, Heaton BE, Konkimalla A, Asakura T, Mikami Y, Fritch EJ, et al. Human lung stem Cell-Based alveolospheres provide insights into SARS-CoV-2-Mediated interferon responses and pneumocyte dysfunction. Cell Stem Cell. 2020;27(6):890–904. e898.
24. Wang C, Hyams B, Allen NC, Cautivo K, Monahan K, Zhou M, Dahlgren MW, Lizama CO, Matthay M, Wolters P, et al. Dysregulated lung stroma drives emphysema exacerbation by potentiating resident lymphocytes to suppress an epithelial stem cell reservoir. Immunity. 2023;56(3):576–91. e510.
25. Sweeney RM, McAuley DF. Acute respiratory distress syndrome. Lancet. 2016;388(10058):2416–30.
26. Thompson BT, Chambers RC, Liu KD. Acute respiratory distress syndrome. N Engl J Med. 2017;377(6):562–72.
27. Boyd DF, Allen EK, Randolph AG, Guo XJ, Weng Y, Sanders CJ, Bajracharya R, Lee NK, Guy CS, Vogel P, et al. Exuberant fibroblast activity compromises lung function via ADAMTS4. Nature. 2020;587(7834):466–71.
28. Liu Q, Liu K, Cui G, Huang X, Yao S, Guo W, Qin Z, Li Y, Yang R, Pu W, et al. Lung regeneration by multipotent stem cells residing at the bronchioalveolar-duct junction. Nat Genet. 2019;51(4):728–38.
29. Barkauskas CE, Cronce MJ, Rackley CR, Bowie EJ, Keene DR, Stripp BR, Randell SH, Noble PW, Hogan BL. Type 2 alveolar cells are stem cells in adult lung. J Clin Invest. 2013;123(7):3025–36.
30. Liu K, Meng X, Liu Z, Tang M, Lv Z, Huang X, Jin H, Han X, Liu X, Pu W, et al. Tracing the origin of alveolar stem cells in lung repair and regeneration. Cell. 2024;187(10):2428–45. e2420.
31. Gautier EL, Shay T, Miller J, Greter M, Jakubzick C, Ivanov S, Helft J, Chow A, Elpek KG, Gordonov S, et al. Gene-expression profiles and transcriptional regulatory pathways that underlie the identity and diversity of mouse tissue macrophages. Nat Immunol. 2012;13(11):1118–28.
32. Fujimori T, Grabiec AM, Kaur M, Bell TJ, Fujino N, Cook PC, Svedberg FR, MacDonald AS, Maciewicz RA, Singh D, et al. The Axl receptor tyrosine kinase is a discriminator of macrophage function in the inflamed lung. Mucosal Immunol. 2015;8(5):1021–30.
33. Mohning MP, Thomas SM, Barthel L, Mould KJ, McCubbrey AL, Frasch SC, Bratton DL, Henson PM, Janssen WJ. Phagocytosis of microparticles by alveolar macrophages during acute lung injury requires MerTK. Am J Physiol Lung Cell Mol Physiol. 2018;314(1):L69–82.
34. Gomez-Lechon MJ. Oncostatin M: signal transduction and biological activity. Life Sci. 1999;65(20):2019–30.
35. Xu P, Yi Y, Xiong L, Luo Y, Xie C, Luo D, Zeng Z, Liu A. Oncostatin m/oncostatin M receptor signal induces Radiation-Induced heart fibrosis by regulating SMAD4 in fibroblast. Int J Radiat Oncol Biol Phys. 2024;118(1):203–17.
36. Cully M. Anti-oncostatin M antibody puts brakes on asthma exacerbations. Nat Rev Drug Discov. 2022;21(3):178.

37. Headland SE, Dengler HS, Xu D, Teng G, Everett C, Ratsimandresy RA, Yan D, Kang J, Ganeshan K, Nazarova EV, et al. Oncostatin M expression induced by bacterial triggers drives airway inflammatory and mucus secretion in severe asthma. Sci Transl Med. 2022;14(627):eabf8188.
38. Mock JR, Garibaldi BT, Aggarwal NR, Jenkins J, Limjunyawong N, Singer BD, Chau E, Rabold R, Files DC, Sidhaye V, et al. Foxp3 + regulatory T cells promote lung epithelial proliferation. Mucosal Immunol. 2014;7(6):1440–51.
39. Dial CF, Tune MK, Doerschuk CM, Mock JR. Foxp3(+) regulatory T cell expression of keratinocyte growth factor enhances lung epithelial proliferation. Am J Respir Cell Mol Biol. 2017;57(2):162–73.
40. Lin SJ, Lo M, Kuo RL, Shih SR, Ojcius DM, Lu J, Lee CK, Chen HC, Lin MY, Leu CM, et al. The pathological effects of CCR2 + inflammatory monocytes are amplified by an IFNAR1-triggered chemokine feedback loop in highly pathogenic influenza infection. J Biomed Sci. 2014;21(1):99.
41. Imhof BA, Aurrand-Lions M. Adhesion mechanisms regulating the migration of monocytes. Nat Rev Immunol. 2004;4(6):432–44.
42. Buch T, Heppner FL, Tertilt C, Heinen TJ, Kremer M, Wunderlich FT, Jung S, Waisman A. A Cre-inducible diphtheria toxin receptor mediates cell lineage ablation after toxin administration. Nat Methods. 2005;2(6):419–26.
43. Scaffidi AK, Mutsaers SE, Moodley YP, McAnulty RJ, Laurent GJ, Thompson PJ, Knight DA. Oncostatin M stimulates proliferation, induces collagen production and inhibits apoptosis of human lung fibroblasts. Br J Pharmacol. 2002;136(5):793–801.

Publisher's Note